Blueprint for All-to-All-Connected Superconducting Spin Qubits

Pita-Vidal, Marta; Wesdorp, Jaap J.; Andersen, Christian Kraglund

DOI
10.1103/PRXQuantum.6.010308

Publication date
2025

Document Version
Final published version

Published in
PRX Quantum

Blueprint for All-to-All-Connected Superconducting Spin Qubits

Marta Pita-Vidal,* Jaap J. Wesdorp, and Christian Kraglund Andersen
QuTech and Kavli Institute of Nanoscience, Delft University of Technology, GA 2600 Delft, Netherlands

(Received 16 May 2024; revised 30 September 2024; accepted 4 December 2024; published 13 January 2025)

Andreev (or superconducting) spin qubits (ASQs) have recently emerged as a promising qubit platform that combines superconducting circuits with semiconductor spin degrees of freedom. While recent experiments have successfully coupled two ASQs, how to realize a scalable architecture for extending this coupling to multiple distant qubits remains an open question. In this work, we resolve this challenge by introducing an architecture that achieves all-to-all connectivity between multiple remote ASQs. Our approach enables selective connectivity between any qubit pair while keeping all other qubit pairs uncoupled. Furthermore, we demonstrate the feasibility of efficient readout using circuit quantum electrodynamics techniques and compare different readout configurations. Our architecture shows promise both for gate-based quantum computing and for analog quantum simulation applications by offering higher qubit connectivity than alternative solid-state platforms.

DOI: 10.1103/PRXQuantum.6.010308

I. INTRODUCTION

To date, two of the most scalable solid-state qubit platforms are semiconducting spin qubits and superconducting qubits. Recent experiments in these architectures have realized systems with tens and hundreds of qubits, respectively [1–9], as well as two-qubit gates with fidelities above 99% [3,10–20]. However, experimental realizations of both platforms are currently limited to low qubit connectivity, often restricted to nearest neighbors in planar grids, and typically featuring at most between three and five connections per qubit [7,9,21–27]. While approaches to increase the connectivity of superconducting qubits via virtual coupling through a bus resonator have been proposed [28–31], the sparse connectivity currently results in a considerable overhead in qubit count, both when it comes to error-correction codes in gate-based quantum computation applications [27,32–34] and to analog quantum simulations [35–39].

An alternative platform to the aforementioned qubits are Andreev (or superconducting) spin qubits (ASQs) [40–47]. These qubits have their state encoded in the spin of a quasiparticle localized within a semiconducting quantum dot that is tunnel coupled to two superconducting leads, thus forming a Josephson junction [40,41]. Recent experimental realizations have explored systems with a single ASQ [43,44] as well as the supercurrent-mediated coupling between two distant ASQs [45]. Yet, no experiments involving more than two ASQs have been reported. Architectures for coupling either adjacent Andreev qubits via wave-function overlap [46] or two distant qubits via virtual photons [48] have been proposed. However, these architectures enable the short-distance coupling of nearest-neighbor qubits in a planar layout plus a reduced number of long-distance links, sharing the same connectivity constraints as semiconducting and superconducting qubits. Thus, it remains an open question if the compact size of ASQs and their strong coupling to the supercurrent can be combined to provide architectural improvements over more conventional solid-state platforms.

Here, we introduce an architecture that offers a solution to the connectivity challenge. Our design allows for the coupling of multiple distant ASQs in a fully connected and scalable way. As a particular example, we demonstrate that this architecture permits selective connectivity between any qubit pair within the system while keeping all other qubit pairs uncoupled. Importantly, the strength of the coupling between two qubits in the system is independent of the distance between them. Furthermore, we illustrate how this system can efficiently perform quantum simulations of highly connected Ising models with a reduced qubit count and a smaller footprint compared to alternative solid-state platforms. The proposed architecture also facilitates sequential, individual, or joint qubit readout. Finally, we outline an experimental protocol for systematically tuning up the system to its operational set point.

*Contact author: marta.pita.vidal@ibm.com

II. CONCEPT

We propose a circuit that consists of a coupling junction, with Josephson energy E_J and phase drop ϕ across it, connected in parallel to a number, N, of ASQs [see Fig. 1(a)]. The subspace of each ASQ is spanned by two spin states, denoted as $|\uparrow_i\rangle$ and $|\downarrow_i\rangle$ for ASQi, where i is the qubit index. This configuration defines N loops through which magnetic fluxes, Φ_i, are threaded, as indicated in Fig. 1(a).

The individual ASQs are implemented using semiconducting quantum dot Josephson junctions [49–56]. The charging energy of each quantum dot is sufficiently large such that the ground-state manifold is composed only of the two singly occupied spin states. Due to the spin-orbit coupling in the semiconductor, each ASQ is characterized by a spin-dependent, in addition to a spin-independent, Josephson energy, denoted as $E_{\mathrm{SO},i}$ and $E_{J,i}$, respectively [41,57]. The values of $E_{\mathrm{SO},i}$ and $E_{J,i}$ can be tuned independently via electrostatic gates for each qubit (not shown in Fig. 1). The Hamiltonian of ASQi can be expressed in terms of these Josephson energies as

$$H_i = E_{J,i}\sigma_i^0 \cos(\phi_i) - E_{\mathrm{SO},i}\sigma_i^z \sin(\phi_i) + \frac{1}{2}\vec{E}_{\mathrm{Z},i}\cdot\vec{\sigma}_i, \quad (1)$$

where $\sigma_i^z = |\uparrow_i\rangle\langle\uparrow_i| - |\downarrow_i\rangle\langle\downarrow_i|$ and $\sigma_i^0 = |\uparrow_i\rangle\langle\uparrow_i| + |\downarrow_i\rangle\langle\downarrow_i|$ denote the Pauli z operator and the identity operator of ASQi, respectively, $\vec{\sigma}_i$ is the vector of Pauli x, y, and z operators of ASQi and $\vec{E}_{\mathrm{Z},i}$ is the externally applied Zeeman field expressed in the coordinate system of ASQi.

To lowest order in $E_{\mathrm{SO},i}/E_J$ and $E_{J,i}/E_J$, the phase drop through the coupling junction becomes $\phi = 0$ and each ϕ_i is determined by the cumulative flux values from 1 to i,

$$\phi_i = \sum_{j=1}^{i} \varphi_j, \quad (2)$$

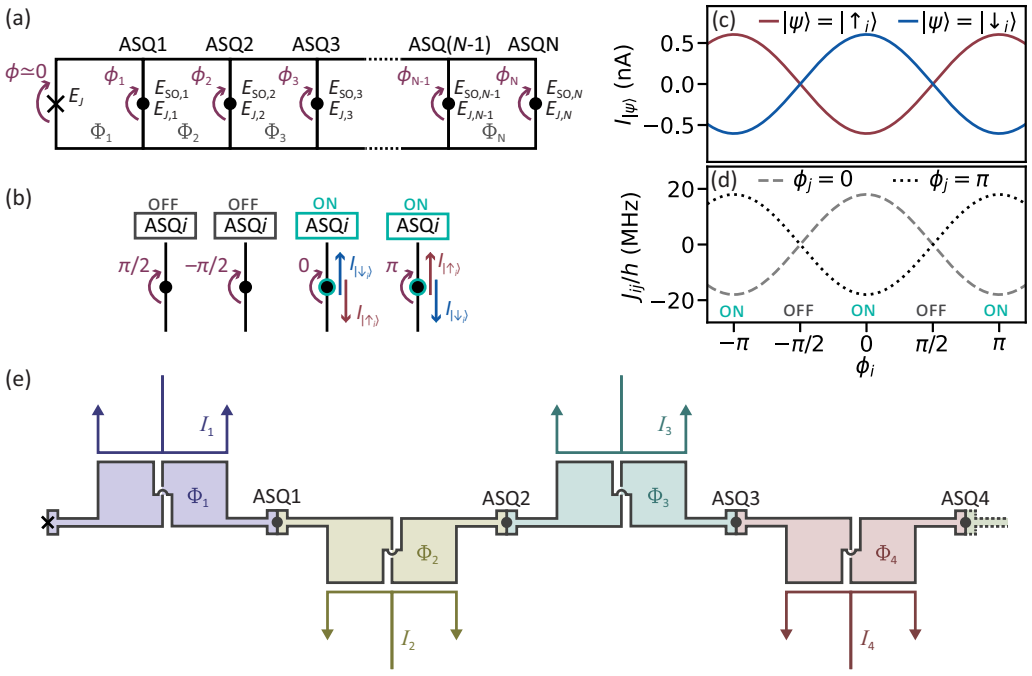

FIG. 1. The scalability of superconducting spin qubits. (a) A circuit diagram of N Andreev spin qubits connected in parallel to a coupling Josephson junction with Josephson energy E_J, thus defining N loops. ASQi has spin-independent and spin-dependent Josephson energies $E_{J,i}$ and $E_{\mathrm{SO},i}$, respectively. The magnetic flux through loop i is denoted as Φ_i. The phase drop across ASQi is denoted as ϕ_i and that across the coupling junction as ϕ. The system is operated in the regime $E_J \gg E_{J,i}, E_{\mathrm{SO},i}$, which results in $\phi \simeq 0$. (b) Diagrams of four possible phase set points for an ASQ. When $\phi_i = \pi/2, -\pi/2$, the spin-dependent component of the supercurrent vanishes and the qubit is labeled as OFF. When, instead, $\phi_i = 0, \pi$ the spin-dependent component of the supercurrent is maximal and the qubit is labeled as ON. We use the notation of $I_{|\uparrow_i\rangle} = \langle\uparrow_i|\mathcal{I}_i|\uparrow_i\rangle$ and $I_{|\downarrow_i\rangle} = \langle\downarrow_i|\mathcal{I}_i|\downarrow_i\rangle$. (c) The supercurrent across ASQi versus the phase drop across it for its two basis states, $|\uparrow_i\rangle$ and $|\downarrow_i\rangle$. Here, we assume $E_{\mathrm{SO},i}/h = 300\,\mathrm{MHz}$, $E_{J,i}/h = 0$ for all ASQs and $E_J/h = 10\,\mathrm{GHz}$. (d) The coupling strength between two ASQs, i and j, versus the phase drop across one of them, ϕ_i [see Eq. (6)], with the same parameters as in (c) and with $\phi_k = 0$ for all other ASQs. The points on the ϕ_i axis with extremal and zero coupling strength are indicated with ON and OFF labels, respectively. (e) An example of a design that minimizes the flux cross-coupling between loops. Each loop is implemented with a twisted gradiometric geometry that renders it insensitive to a global magnetic field. The two subloops of each loop, shaded with the same color, have identical areas. The magnetic flux through each loop is controlled with a flux-bias line, indicated with a hue-matching line.

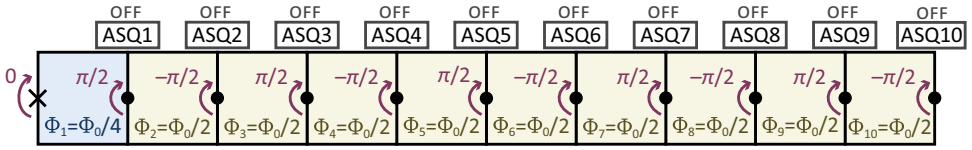

FIG. 2. The idling flux configuration. A chain with $N = 10$ showing the flux set point for an idling configuration in which all qubits are uncoupled. The choice of $\Phi_1 = \Phi_0/4$ and $\Phi_i = \Phi_0/2$ for all other loops sets alternating phase drops of $\pi/2$ and $-\pi/2$ for all qubits.

where $\varphi_i = 2\pi\Phi_i/\Phi_0$, $\Phi_0 = h/(2e)$ is the magnetic flux quantum, h is the Planck constant, and e is the absolute value of the electron charge. Therefore, by controlling the external fluxes, one can independently fix the values of all phase drops, ϕ_i. Taking the phase derivative of the ASQ Hamiltonian [Eq. (1)] and assuming a magnetic field aligned with the spin-polarization direction, $\vec{E}_{Z,i} \cdot \vec{\sigma}_i = E_{Z,i}\sigma_i^z$, we obtain its current operator,

$$\mathcal{I}_i = \frac{\pi}{\Phi_0}\frac{\partial H_i}{\partial \phi_i} = \frac{I_{s,i}}{2}\sigma_i^z + I_{0,i}\sigma_i^0, \tag{3}$$

where $I_{0,i} = (-\pi/\Phi_0)E_{J,i}\sin(\phi_i)$ represents the spin-independent component and the spin-dependent supercurrent is

$$I_{s,i} = \frac{-2\pi}{\Phi_0}E_{SO,i}\cos(\phi_i)\,. \tag{4}$$

Notably, when ϕ_i is either $\pi/2$ or $-\pi/2$, $I_{s,i}$ vanishes, rendering the supercurrent identical for both qubit states [see Fig. 1(c)]. On the contrary, when ϕ_i is either 0 or π, the magnitude of the spin-dependent component of the supercurrent is maximal. Throughout this paper, we refer to these two flux set points as OFF and ON, respectively, as depicted in Fig. 1(b).

The circuit can be implemented in practice with independent control over the individual fluxes and with maximal addressability using the implementation illustrated in Fig. 1(e). Each loop is implemented with a twisted gradiometric loop geometry similar to the experimental implementation in Ref. [45]. Each loop is inductively coupled to a flux-bias line with current I_i and a symmetrical design at its end, where currents flow in opposite directions. This combination of the loop and flux-bias line designs maximizes their mutual inductance while minimizing unwanted cross-coupling to other loops. First, the two opposite currents on the flux line induce contributions to the flux through the loop that add up due to its twisted geometry. Second, the generated magnetic field decreases with distance faster than for monopole flux-line configurations, resulting in reduced magnetic fields at the locations of other loops. Third, the gradiometric loop design reduces the sensitivity to homogeneous fields, again reducing the unwanted cross-coupling, as well as the sensitivity to global magnetic noise.

We note that the suggested arrangement imposes less strict line routing constraints compared to other solid-state qubit platforms. A two-dimensional arrangement of semiconducting spin qubits requires the use of multilayer gates [2,58], while typical superconducting qubit chips require through-silicon vias [59], air bridges [60,61], or a flip-chip configuration [62] to manage line crossing. In contrast, the proposed ASQ system is arranged linearly, allowing gate and flux lines access from top and bottom, without line-crossing issues, as shown in Fig. 1(e). We note, however, that a flip-chip [63] architecture could still be beneficial for separating the readout superconducting circuitry (see Sec. V) from the qubit chip in ASQ implementations using Si-Ge substrates, although implementations of superconducting qubits and resonators have also been demonstrated on Si-Ge substrates [64,65].

We envision two possible driving mechanisms [42,66–68]: either using the flux-bias lines for driving the spin-flip transitions via their supercurrent-matrix element or applying microwave-frequency pulses to the electrostatic gates of each qubit, which induces spin transitions via the electric dipole spin resonance (EDSR) mechanism [69,70]. The supercurrent- and charge-matrix elements are minimal and maximal, respectively, at the OFF flux set point [67]. Consequently, we see gate driving as the preferred driving method to allow for simultaneous single-qubit operation of different qubits.

The interactions between all pairs of qubits can be adjusted by varying the flux set points. For example, an idling configuration where all qubits are OFF is shown in Fig. 2. By setting $\Phi_1 = \Phi_0/4$, ASQ1 is set to its OFF state, with $\phi_1 = \pi/2$, i.e., the qubit does not interact with any other qubit. In turn, $\Phi_i = \Phi_0/2$ for the remaining loops results in alternating phase drops of $\pi/2$ and $-\pi/2$ for all other ASQs, rendering them OFF as well. Consequently, in this configuration all qubits are uncoupled.

III. ALL-TO-ALL SELECTIVE COUPLING

Next, we discuss the full circuit Hamiltonian and how we can control the interactions between multiple ASQs. When either the Zeeman energy is low, $|\vec{E}_{Z,i}| \ll E_{SO,i}$, or the external magnetic field is applied along the spin-polarization direction for all qubits, $\vec{E}_{Z,i} = E_{Z,i}\sigma_i^z$, the qubits become pairwise longitudinally coupled to each

other [71], as first discussed in Ref. [41] for the case of $N = 2$ and experimentally realized in Ref. [45]. In this situation, the Hamiltonian describing the longitudinally coupled system can be expressed in the ASQ basis as

$$H_{\mathrm{ASQ}} = \sum_{i=1}^{N} \left(\frac{1}{2} E_i \sigma_i^z + \sum_{j<i} \frac{1}{2} J_{ij} \sigma_i^z \sigma_j^z \right), \tag{5}$$

where $E_i = -2E_{\mathrm{SO},i} \sin(\phi_i) + E_{\mathrm{Z},i}$ is the energy of qubit i and J_{ij} represents the longitudinal coupling energy between qubits i and j. In Eq. (5) and for the remainder of this section, we have disregarded spin-independent terms, as they have no influence on the spin dynamics. Following Ref. [41] (see also Appendix A), the coupling strength is, to first order in $E_{\mathrm{SO},i}/E_J$, given by

$$J_{ij} = -2 \frac{E_{\mathrm{SO},i} E_{\mathrm{SO},j}}{|\tilde{E}|} \cos\left(\sum_{k=1}^{i} \varphi_k - \varphi_{\tilde{E}} \right) \times \cos\left(\sum_{k=1}^{j} \varphi_k - \varphi_{\tilde{E}} \right), \tag{6}$$

where

$$\tilde{E} = E_J + \sum_{l=1}^{N} E_{J,l} e^{i \sum_{k=1}^{l} \varphi_k} \tag{7}$$

is the total spin-independent Josephson energy of the system and $\varphi_{\tilde{E}}$ is the argument of $\tilde{E}$.

In the limit of $E_{J,i}/E_J \to 0$, the phase-offset $\varphi_{\tilde{E}}$ vanishes. In such scenario, it directly follows from Eq. (6) that, when two qubits are ON (with $\sum_{k=1}^{i} \varphi_k = 0, \pi$), the coupling between them is maximal. Conversely, when either one of the two qubits is OFF (with $\sum_{k=1}^{i} \varphi_k = \pm\pi/2$), the coupling between them becomes zero, as illustrated in Figs. 3(a) and 3(b) for two possible flux configurations.

Away from the limit of $E_{J,i}/E_J \to 0$, the ON and OFF flux set points deviate from their exact values of 0, π, and $\pm\pi/2$, respectively. The offset is $\varphi_{\tilde{E}}$, which depends on the global flux configuration and, importantly, can be independently measured. Therefore, each individual flux can still be set to either maximize or turn off the couplings between any pair. At this point, it is interesting to note that when we adjust the flux configuration to the corrected flux set points, there is no unwanted coupling arising from the nonzero values of $E_{J,i}$. The effect of $E_{J,i}$, on the other hand, is to reduce the magnitude of the wanted coupling when their values become comparable to E_J.

From Eq. (6), we calculate the coupling strength between any selected pair of qubits; see Figs. 3(c) and 3(d) for two examples with realistic parameter sets, with $N = 10$ and $N = 30$, respectively. We find ON-ON coupling strengths of around 10 MHz that slowly decrease with increasing E_J. The couplings are calculated here for a situation in which two qubits, ASQn and ASQm, are coupled to each other while the rest of the qubits are kept near their corrected OFF flux set points but deviate from them, each by a random value drawn from a uniform distribution between plus and minus $0.001\Phi_0$. For typical experimental implementations, these deviations correspond to errors in the flux-bias lines currents of less 10 μA [45,72], well above the resolution of typical current sources [73] and thus well within experimental reach. The unwanted ON-OFF and OFF-OFF couplings resulting from these imprecise flux settings remain significantly lower than the ON-ON coupling strength, by around 2 and 4 orders of magnitude, respectively, and can be reduced further by more precise flux control.

By flux pulsing, this selective coupling scheme enables the implementation of controlled-phase (CPHASE) gates between any qubit pair within the system [74]. In particular, coupling strengths of more than 10 MHz, in combination with virtual corrections to the single-qubit phases [75], would allow us to realize a CPHASE gate in less than $h/(4J) = 25$ ns. Starting from an idling configuration, only the fluxes of the loops adjacent to the two selected qubits must be swept to reach the coupling configuration shown in Figs. 3(a) and 3(b). Importantly, during pulsing, the two fluxes adjacent to qubit m must be adjusted simultaneously to prevent undesired coupling between qubits m and $m + 1$.

Based on previous demonstrations on different qubit platforms [76,77], we anticipate that tuning two qubits from their OFF to their ON flux set points, and back, can be achieved within 10–20 ns. This fast flux pulsing would allow for the implementation of a 25-ns CPHASE gate. Additionally, spin-orbit interaction enables fast single-qubit manipulation of ASQs. In particular, $\pi/2$ and π single-qubit rotations have previously been demonstrated in 2 ns and 4 ns, respectively [44]. These fast single- and two-qubit gates render ASQs a competitive qubit platform, with gate speeds on par with other state-of-the-art superconducting- and spin-qubit processors.

IV. QUANTUM SIMULATION OF HIGHLY CONNECTED ISING SYSTEMS

Beyond its use for digital gate-based quantum computation schemes, the system introduced in Fig. 1 holds potential for applications in analog quantum simulation. The Hamiltonian presented in Eq. (5), which corresponds to either a reduced Zeeman field or a Zeeman field aligned with all qubits, directly maps the Hamiltonian of an all-to-all longitudinally connected Ising model. More generally, when the Zeeman field has $E_{\mathrm{Z},i}^x \geq E_{\mathrm{SO},i}$ components perpendicular to the spin directions, $\vec{E}_{\mathrm{Z},i} = E_{\mathrm{Z},i}^z \sigma_i^z + E_{\mathrm{Z},i}^x \sigma_i^x$,

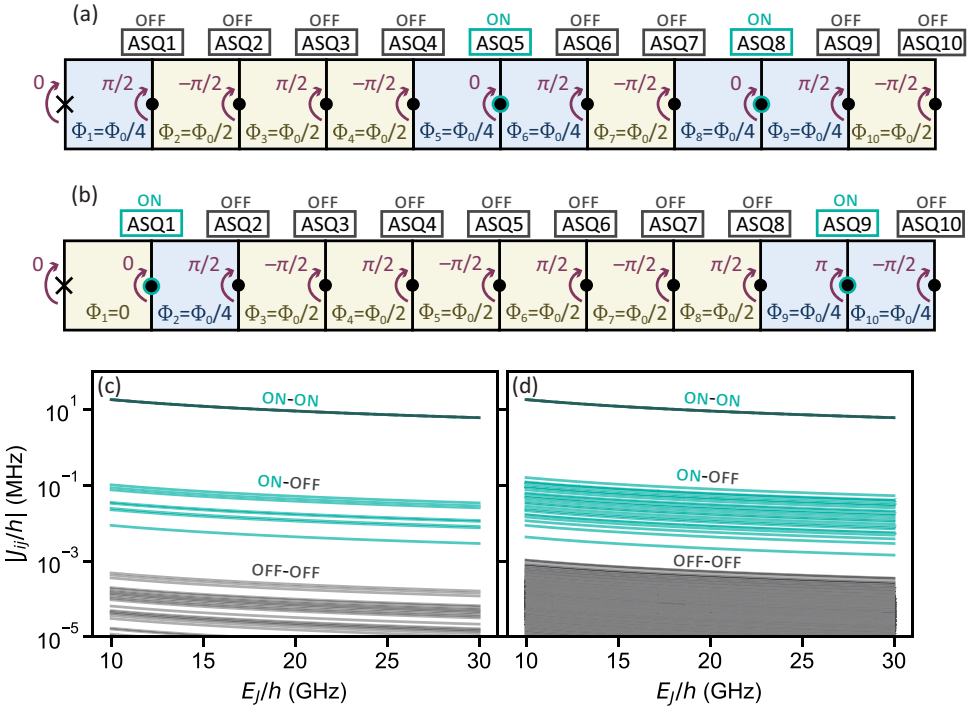

FIG. 3. All-to-all selective coupling. (a),(b) Two chains with $N = 10$, showing two example flux set points needed for selective two-qubit coupling between (a) qubits 5 and 8 and (b) qubits 1 and 9. In contrast to the idling configuration of Fig. 1(c), the phase drops across the two selected qubits, labeled as ON, are either 0 or π, thus maximizing their spin-dependent supercurrent. In these configurations, the rest of the qubits remain uncoupled. (c),(d) The absolute value of the qubit-qubit coupling strength, $|J_{ij}|$, obtained from Eq. (6), for two parameter configurations, with random offsets added to the ideal flux-bias points. For each panel, the dark green line indicates the coupling strengths between the two qubits that are ON, n and m, the light green lines indicate the (undesired) coupling strengths between either n or m and another qubit, and the gray lines indicate the (undesired) coupling strength between any other pair of qubits. (c) For $N = 10$, $n = 3$, $m = 8$, $E_{\mathrm{SO},i}/h = 300\,\mathrm{MHz}$, and $E_{J,i}/h = 0$ for all ASQs. The fluxes deviate from their ideal values by amounts $\Delta\Phi_i$ that take random values from a uniform distribution between plus and minus $0.001\Phi_0$. (d) The same as (c) but for $N = 30$, $n = 6$, and $m = 18$.

the coupling Hamiltonian also includes transverse $\sigma_i^x\sigma_j^x$, as well as $\sigma_i^x\sigma_j^z$ and $\sigma_i^z\sigma_j^x$, coupling terms (see Appendix B):

$$H_{\mathrm{ASQ}} = \sum_{i=1}^{N}\left(\frac{E_i}{2}\sigma_i^z + \sum_{j<i}\left(\frac{J_{ij}^{zz}}{2}\sigma_i^z\sigma_j^z + \right.\right. \tag{8}$$

$$\left.\left. + \frac{J_{ij}^{xx}}{2}\sigma_i^x\sigma_j^x + \frac{J_{ij}^{xz}}{2}\sigma_i^x\sigma_j^z + \frac{J_{ij}^{zx}}{2}\sigma_i^z\sigma_j^x\right)\right). \tag{9}$$

Here, J_{ij}^{zz} and J_{ij}^{xx} denote the longitudinal and transverse coupling energies, respectively.

Classically, efficient simulation is possible only for sparsely connected longitudinal systems with planar couplings. However, when either transverse terms are present in a planar system or the system exhibits higher connectivity, only nondeterministic polynomial-time (NP)-hard classical exact solutions exist [78]. Flux-qubit systems have been used to approach the solution of some problems using quantum annealing [79–81]. Nonetheless, these quantum annealers have sparse connectivity, which requires an initial embedding of the desired problem into the qubit system at the cost of an increased number of physical qubits [35]. Due to their high connectivity, as we have introduced here, Andreev spin qubits constitute a promising solid-state platform well suited for simulating a broader range of problems without requiring additional overhead in terms of qubits. Besides applications in quantum annealing, this system can be used to explore the Ising spin dynamics without the need for Trotterization [5]. The system presented here extends the range of Ising problems that can be simulated to encompass all partitioning problems, defined by $J_{ij}^{zz} = a_i^z a_j^z$, $J_{ij}^{xz} = a_i^x a_j^z$, $J_{ij}^{zx} = a_i^z a_j^x$, and $J_{ij}^{xx} = a_i^x a_j^x$. However, a generic longitudinal Ising system has a total of $(N^2 - N)/2$ independent couplings, meaning that the ASQ system studied here, with N free flux parameters, cannot simulate all possible connectivity configurations of the Ising model. Note that the tuning of the system from its fully uncoupled idling state (Fig. 2) to a fully coupled state [Fig. 4(a) or Fig. 4(b)], only requires the adjustment of the flux through loop 1 by a quarter of a flux

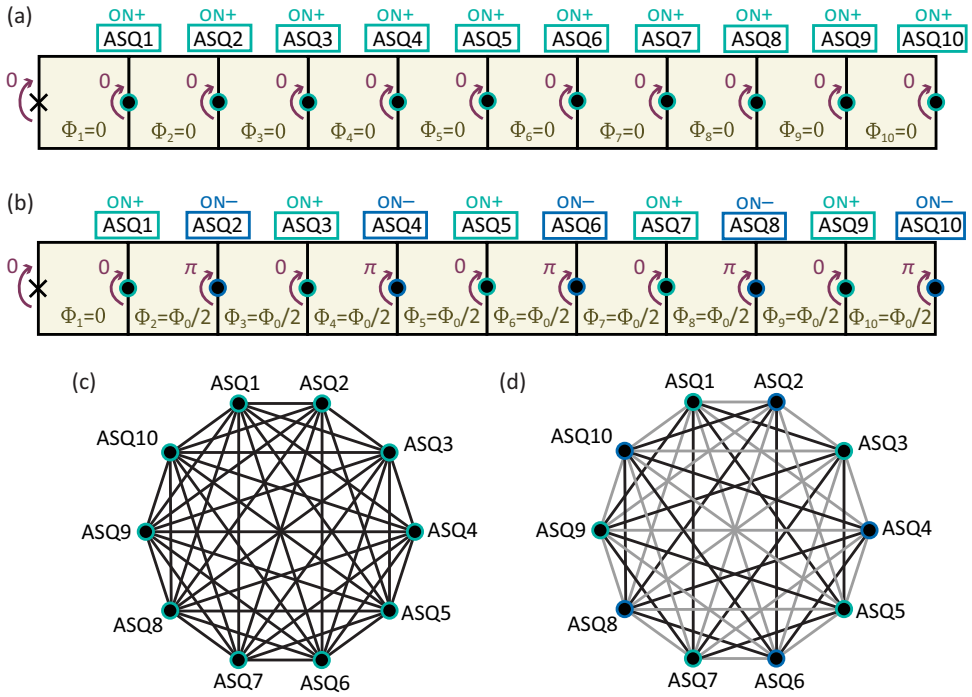

FIG. 4. Quantum simulation with ASQs. (a),(b) Circuit diagrams for $N = 10$ exemplifying two flux configurations in which all qubits are coupled to each other, thus mapping a highly connected Ising system. (c),(d) Graph diagrams indicating the couplings (edges) between each pair of qubits (nodes). Panels (c) and (d) correspond to the flux configurations depicted in (a) and (b), respectively. For (c), all coupling strengths have equal sign $J_{ij} = -|J_{ij}|$ (black edges). For (d), the coupling strengths have either a negative sign, $J_{ij} = -|J_{ij}|$ if $|i-j| = 2n$ (black edges), or a positive sign, $J_{ij} = +|J_{ij}|$ if $|i-j| = 2n+1$ (gray edges), where n is an integer number.

quantum. This provides straightforward control over the evolution time of an analog quantum simulation by only pulsing a single flux line.

V. READOUT

The spin-supercurrent coupling of superconducting spin qubits provides a means for reading out their state through the use of circuit quantum electrodynamics techniques [42,57,82–84]. In this section, we detail different readout alternatives that depend on the readout circuitry and on the specific qubits that need to be measured. In Sec. V A, we present a protocol for sequentially reading out the state of all qubits in the computational basis for a scenario in which the magnetic field is parallel to all qubits. This can be achieved using either a transmon or a fluxonium circuit [85]. Subsequently, in Sec. V B, we present a means to selectively read out the state of a single qubit while keeping all qubits uncoupled. Lastly, in Sec. V C, we instead present the joint readout of multiple qubits to determine the total number of qubits that are in their excited state. Note that in all cases, the readout circuit must be detuned from all ASQ frequencies to prevent transverse coupling between the qubits and the readout. Moreover, for all readout protocols, the readout circuit must stay in its ground state during readout. This requires the readout resonator to be in the few-photon regime, analogous to the situation for readout of other superconducting circuits [86,87].

A. Sequential readout of all qubits

The resonator and transmon circuits used to read out the spin in previous work are sensitive to the ASQ inductance [43–45,57,82–84]. As a result, these circuits are maximally sensitive to an ASQ state when the ASQ is in its OFF set point and fully insensitive to it when the set point is ON. In the absence of a magnetic field or under the presence of a magnetic field parallel to all qubits, if all qubits are set to their ON set point, they are fully uncoupled from the readout circuit but they are also maximally longitudinally coupled to each other. In this case, their relative phases rotate over time but the population in each computational basis state remains conserved as the coupling is longitudinal, thus preserving the measurement result. As illustrated in Fig. 5, we can use this idea for reading out each of the qubits, by sequentially switching all of the ASQs to their OFF set point one by one [an example for qubit 5 is shown in Fig. 5(a)], since an ASQ at its OFF set point couples strongly to the readout circuit. We discuss two alternative circuits for selectively reading out the state of a qubit when it is OFF while being insensitive to the states of the qubits that are ON.

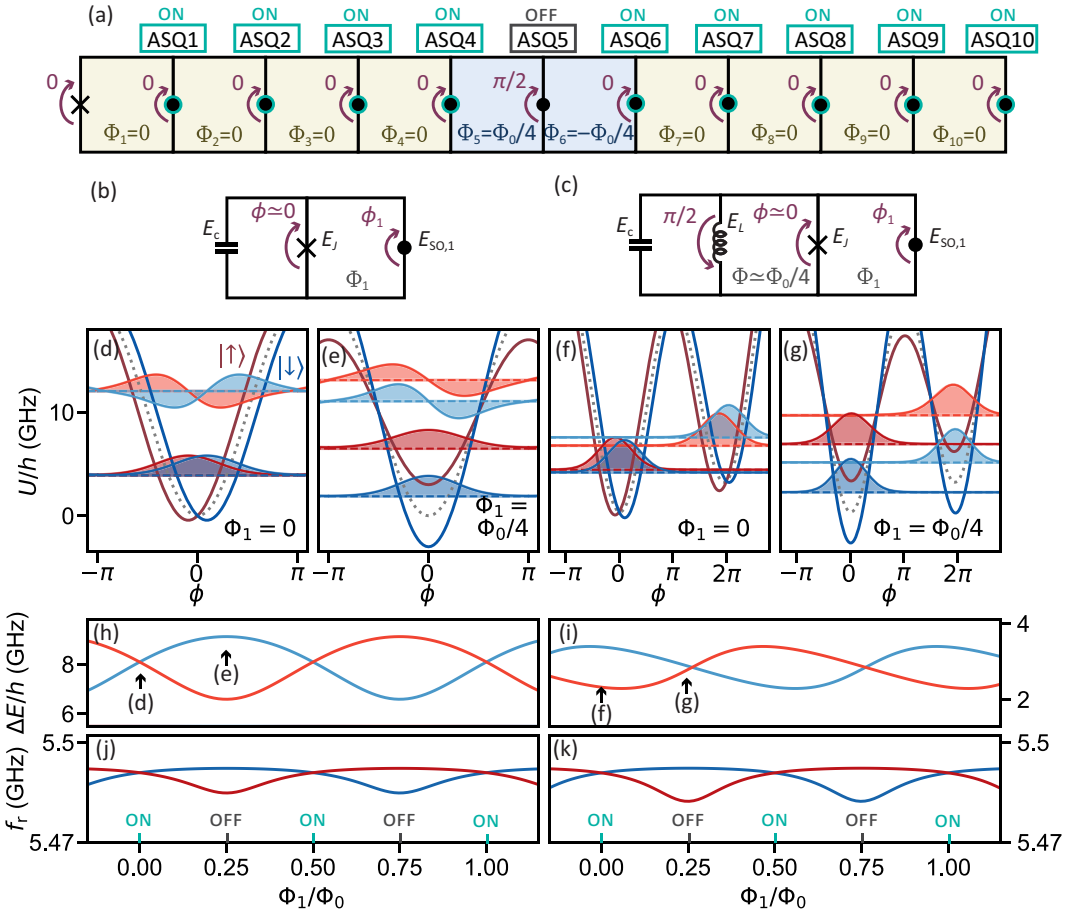

FIG. 5. Sequential readout of qubits at their OFF set point. (a) The circuit for reading out the state of qubit 5. All qubits except for ASQ5 are ON. The phase drop $\phi_5 \sim \pi/2$ sets ASQ5 OFF. (b),(c) Two alternative readout circuits, shown for the case $N = 1$ for simplicity. (b) The transmon-readout circuit diagram. A capacitor with charging energy E_c is connected in parallel to the coupling junction and the Andreev spin qubit. (c) The fluxonium-readout circuit diagram, also including an inductor with inductive energy E_L connected in parallel. The inductor and the coupling junction define a loop with magnetic flux Φ through it. (d),(e) The transmon potential versus the phase drop across the coupling junction, ϕ, for $\Phi_1 = 0$ (ON) and $\Phi_1 = \Phi_0/4$ (OFF), respectively. In both cases, $E_{J,1} = 0$, $E_c/h = 1.0$ GHz and $E_J/h = 10.0$ GHz. The dotted lines indicate the case $E_{SO,1} = 0$. The colored lines indicate the two possible potentials depending on the state of the ASQ, for $E_{SO,1}/h = 3$ GHz. The color-filled regions represent the wave functions of the two lowest-energy scales in each case, in arbitrary units. (f),(g) The same as (d),(e) but for the fluxonium circuit with $E_L/h = 0.3$ GHz and at $\Phi = \Phi_0/4$. (h) The first transmon transition frequency versus the flux for the two possible spin states, $|\uparrow\rangle$ and $|\downarrow\rangle$, indicated with red and blue, respectively. (j) The frequency of a readout resonator with bare frequency $f_{r,0} = 5.5$ GHz capacitively coupled to the transmon with a resonator-transmon coupling strength $g/h = 200$ MHz. (i) The first fluxonium transition versus the flux for the two possible spin states. (k) The same as (j) but for a readout resonator capacitively coupled to the fluxonium with resonator-fluxonium coupling strength $g/h = 200$ MHz.

1. Transmon readout

The first approach employs a transmon circuit [67,88,89], as depicted in Fig. 5(b), for simplicity for the case $N = 1$. The transmon consists of a capacitor, with charging energy E_c, connected in parallel to the coupling and ASQ junctions. Its Hamiltonian can be expressed as

$$H_t = -4E_c(\hat{n} - n_g)^2 + E_J(1 - \cos(\phi)) + H_{ASQ}(\phi), \tag{10}$$

where $H_{ASQ}(\phi)$ denotes the Hamiltonian of all ASQs in parallel, now including the spin-independent parts, which depends on all fluxes. $\hat{n}$ is the conjugate charge of ϕ and n_g is the offset charge in the transmon island, expressed in units of the Cooper-pair charge $2e$.

As shown in Fig. 5(d), when an ASQ is at its ON set point ($\varphi_1 = 0$), the eigenstates of the transmon have the same energy independently of the qubit state ($|\uparrow\rangle$ or $|\downarrow\rangle$). Consequently, the transmon transition frequencies are identical for both qubit states [see Fig. 5(h)]. If the ASQ is instead at its OFF set point, the transmon eigenenergies change depending on the qubit state [red and blue in Fig. 5(e)] [44,90]. In Fig. 5(j), we show the resulting frequencies of a readout resonator capacitively coupled to the transmon

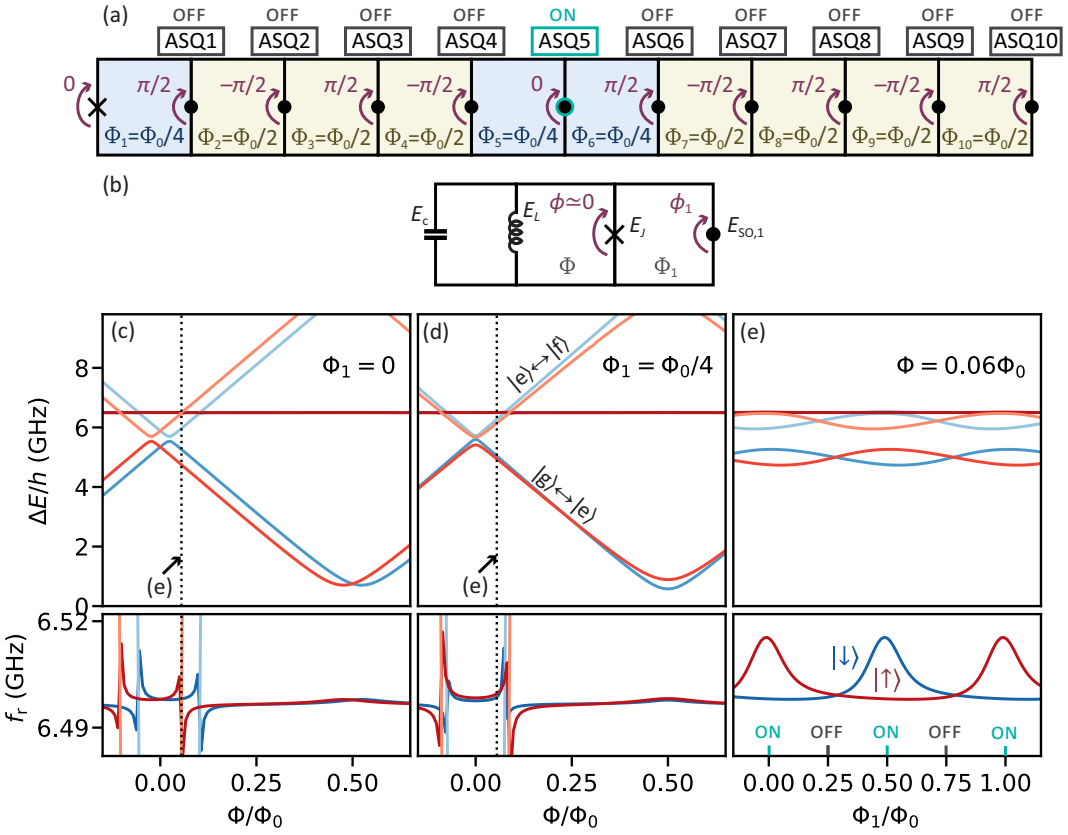

FIG. 6. The selective readout of a qubit at its ON set point. (a) The circuit diagram for $N = 10$, exemplifying the flux configuration for reading out the state of qubit 5. The phase drop $\phi_5 \sim 0$ sets ASQ5 ON, while all other qubits are OFF and thus uncoupled. (b) The same as Fig. 5(c). In this case, the value of Φ is not fixed. $E_c/h = 4.0\,\text{GHz}$, $E_{SO,1}/h = 1.5\,\text{GHz}$, $f_{r,0} = 6.6\,\text{GHz}$, $g/h = 300\,\text{MHz}$, and the other parameters are the same as in Fig. 5. (c)–(e) The frequencies of the fluxonium (top) and of a resonator capacitively coupled to it (bottom) for different flux configurations: (c) $\Phi_1 = 0$; (d) $\Phi_1 = \Phi_0/4$; (e) $\Phi = 0.06\Phi_0$. For (c) and (d), the ASQ is ON and OFF, respectively. As Φ is varied, there are different anticrossings between the resonator and the second fluxonium transition. (e) The Φ_1 dependence when Φ is fixed near one of such anticrossings, at the value indicated with a vertical dotted line in (c) and (d). This results in equal resonator frequencies when the ASQ is OFF and in different resonator frequencies when it is ON.

with a coupling energy g. The resonator frequencies are different when the qubit is at its OFF set point and identical when it is ON, thus allowing us to selectively read out the state of individual OFF qubits. The difference between the two resonator frequencies is then the effective dispersive shift from the ASQ. For the parameters used in Fig. 5, we find a maximal effective dispersive shift of 7.4 MHz.

2. *Fluxonium readout*

An alternative readout circuit to realize the same protocol is a fluxonium circuit [91], shown in Fig. 5(c). Its Hamiltonian can be expressed as

$$H_f = -4E_c\hat{n}^2 + \frac{1}{2}E_L(\phi - \varphi)^2 + E_J\,(1 - \cos(\phi)) + H_{\text{ASQ}}(\phi), \tag{11}$$

where E_L is the inductive energy of the fluxonium shunting inductor and $\varphi = 2\pi\Phi/\Phi_0$ denotes the reduced flux through the loop formed by the inductor and the coupling junction. If the fluxonium flux is set to $\varphi = \pi/2$, the circuit can be used to selectively read out qubits at their OFF set point, analogously to the transmon case [see Figs. 5(f), 5(g), 5(i), and 5(k)]. Note that, due to the complexity of the dispersive shifts in a resonator-fluxonium system [92], the resonator dispersion [Fig. 5(i)] does not follow the dispersion of the lowest-energy fluxonium transition [Fig. 5(k)].

B. Selective readout of one qubit

In certain applications, such as ancilla-based parity readout, there is a need to selectively read out the state of an individual qubit without affecting any other qubits. To facilitate this selective readout, we introduce the protocol illustrated in Fig. 6. This method consists of configuring all qubits to their OFF set points, ensuring that they remain uncoupled. Simultaneously, the specific qubit that needs to be measured is set to its ON set point [see Fig. 6(a)]. As

only one qubit is ON, it does not interact with any of the other qubits.

As discussed in the previous section, a qubit that is ON cannot be read out using the inductance-sensitive readout circuits presented in Fig. 5. Instead, we use a fluxonium circuit such as the one shown in Fig. 6(b). This circuit is tuned to a precise flux φ set point positioned near an avoided crossing between a higher-order fluxonium transition and the readout resonator. In fact, fluxonium qubits often get most of their dispersive shift from interactions with higher-lying states [92,93]. In Figs. 6(c) and 6(d), we show an avoided crossing between the second fluxonium transition and the readout resonator as φ is varied, for the ON and OFF ASQ set points, respectively. By setting φ close to this avoided crossing, the frequency of the readout resonator depends on the ASQ state when the ASQ is ON and remains unaffected when it is OFF. This approach enables the selective readout of the state of an individual qubit at the ON set point while being insensitive to all other qubits that are at the OFF set point. Note, however, that there is a balance between the proximity to the avoided crossing and the number of readout photons, as the closer the flux point is to the avoided crossing, the higher is the hybridization between the readout resonator and the fluxonium states [94].

C. Joint readout of all qubits

In situations in which the $E_{\mathrm{SO},i}$ values of all qubits are similar, there is a third readout option available, which allows differentiation between various joint states based on the total number of qubits that are in their $|\uparrow_i\rangle$ state. This joint-readout protocol entails configuring all qubits to their OFF flux set points, which leaves them uncoupled and thereby does not affect their state, and using the inductance-sensitive readout circuits introduced in Figs. 5(b) and 5(c). As a result, all joint states with the same number of qubits in their $|\uparrow_i\rangle$ state lead to the same dispersive shift on the resonator. In total, there are N different resonator frequencies, each corresponding to a different total number of $|\uparrow_i\rangle$ spins. This configuration has several potential applications:

(1) *Direct counting of excited qubits.* If the dispersive shifts and resonator line width are designed so that the N resulting readout signals can be distinguished, this configuration allows for the direct count of the total number of qubits in their $|\uparrow_i\rangle$ state.

(2) *Measurement-induced state initialization.* By selecting a specific readout frequency to distinguish the $|\downarrow_0\downarrow_1\cdots\downarrow_N\rangle$ state from all other states, this approach can be employed for state preparation, to herald the system in this state [95,96]. Such techniques can also be used to herald entangled states [97].

(3) *Fidelity benchmarking of quantum gates.* The ability to differentiate the $|\downarrow_0\downarrow_1\cdots\downarrow_N\rangle$ state from all other states can be used to benchmark gate sequences that should have the global ground state as their final state, such as randomized benchmarking protocols [98].

(4) *Quantum simulation.* Finally, in quantum simulation, distinguishing states with a fixed number of $|\uparrow_i\rangle$ spins from all other states can be useful to verify if the final state falls within the correct subspace, confirming the accuracy of the simulation [99].

These diverse applications underline the versatility of the ASQ system. However, further research is essential to address specific implementation details.

VI. TUNE-UP PROTOCOL

To demonstrate the viability of this proposal, we now discuss a tuning protocol assuming the physical realization of ASQs as done in Refs. [43–45]. Implementing each Andreev spin qubit in a semiconducting Josephson junction permits pinching it off (i.e., setting both of its Josephson energies to zero) by electrostatic gating. In this section, we explain how, by selectively pinching off different combinations of qubits, the global system can be sequentially tuned up to its operational configuration, as depicted in Fig. 7.

The tune-up process follows the procedure outlined in Ref. [45,57] for the $N = 1$ and $N = 2$ cases, respectively. In the initial step, illustrated in Fig. 7(a), all ASQs are pinched off and the coupling junction is characterized. As the E_{c} and E_L values are known by design, the value of E_J can be determined from the measured frequency of the transmon or fluxonium-readout circuitry. If the coupling junction is implemented with a semiconducting Josephson junction, E_J can be electrostatically set at this step to a target value much larger than the target value for $E_{\mathrm{SO},i}$ and $E_{J,i}$.

Subsequent steps involve selectively pinching off all ASQs except one, allowing it to be tuned up independently. This configuration is shown in Figs. 7(b)–7(d) for qubits 1, 2, and 3, respectively. This sequential approach permits the independent investigation of the gate and magnetic field dependencies of each qubit, enabling the selection of an optimal gate set point. Note that as opposed to semiconducting spin qubits, where capacitive crosstalk between the electrostatic gates of adjacent qubits requires defining virtual gates [100,101], we do not expect the ASQ architecture suggested here to suffer from significant gate crosstalk, thus simplifying the system tune-up. Any small residual crosstalk can be accommodated by iteratively fine tuning the electrostatic gates of all the qubits one by one.

Initially, the gate space is mapped out at zero magnetic field to identify regions with sizable $E_{\mathrm{SO},i}$ and low

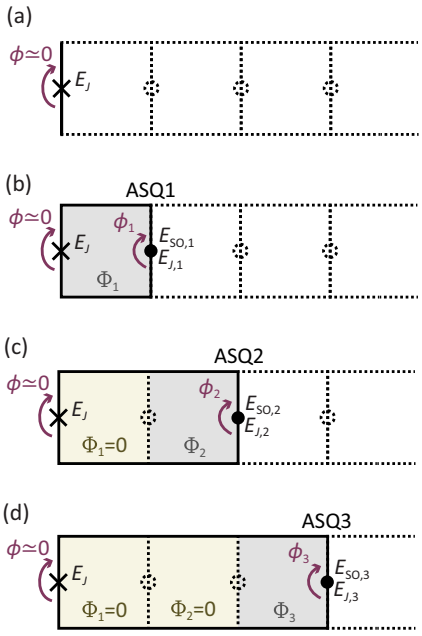

FIG. 7. Sequential qubit tune-up. Each panel shows the circuit diagram of the loop array in different configurations, at subsequent steps in the tune-up process. (a) All qubits are pinched off with their electrostatic gates so that $E_{\mathrm{SO},i} = E_{J,i} = 0$. In this configuration, there are no loops and the value of E_J can be directly determined. (b) While keeping the rest of ASQs pinched off, ASQ1 is tuned up with its electrostatic gates following the procedure described in Ref. [57]. This allows us to fix the desired values of $E_{\mathrm{SO},1}$ and $E_{J,1}$, as well as to determine the I_1 set points that set $\Phi_1 = 0$ and Φ_0. (c) Subsequently, the flux set point of ASQ1 is fixed at $\Phi_1 = 0$ and the electrostatic gates of ASQ1 are pinched off. Following a procedure analogous to that in (b), one can set the values of $E_{\mathrm{SO},2}$ and $E_{J,2}$ and determine the I_2 set points that set $\Phi_2 = 0$ and Φ_0. (d) The same as (b) and (c) but for ASQ3.

$E_{J,i}$. This optimization aims at maximizing the coupling strength [see Eq. (6)]. An efficient way to perform this mapping is by detecting a frequency splitting of the readout resonator at fixed ASQ flux points (see Sec. V).

Subsequently, the magnetic field is set to a nonzero value, allowing for the investigation of the magnetic field dependence. This step provides access to the spin-polarization direction and the g factor at each gate set point.

During operation, the global magnetic field will be fixed at a predetermined value and direction, chosen to align with the chip plane to maximize the magnetic field resilience of the readout circuitry [102–106]. Therefore, for each ASQ, a gate set point is selected so that the spin-polarization direction aligns with the preferred direction relative to the chosen magnetic field operation direction. This relative alignment depends on the application. For gate-based quantum computing, the operation is simplified if only longitudinal coupling terms are present [as in Eq. (5)]. Thus, the spin direction must either be chosen to be aligned with the magnetic field direction or, alternatively, the system can be operated under magnetic field strengths much lower than $E_{\mathrm{SO},i}$. The latter option avoids the need for the spin-polarization directions of all ASQs to be aligned with each other, thus simplifying the system tune-up, and at the same time reduces the charge-noise sensitivity [107]. For quantum simulation of Ising systems, however, the spin direction can be adjusted to determine the ratio between longitudinal and transverse coupling terms. A consideration regarding the g factors is that the qubit frequencies should not match the frequencies of the readout resonator or the readout superconducting qubit and that they lie within an experimentally accessible frequency band. For InAs-based devices, typical g-factor values range from 2 to 16 [57,84,108]. This corresponds to frequencies between 1.5 and 11.2 GHz for an applied magnetic field of 50 mT. The frequencies of physically nearby qubits are chosen so that they do not overlap, to avoid possible drive crosstalk during operation. Once the set point for one qubit is determined in this manner, its junction can be pinched off, and the next qubit can be characterized and tuned up similarly.

The change in the global magnetic field during the preceding steps alters the $\Phi_i(I_i)$ mappings. Additionally, there might be unwanted flux crosstalk between nearby loops. Therefore, all $\Phi_j(I_i)$ mappings can be determined in a subsequent round of tune-up steps, carried out after fixing the global magnetic field at its operational set point. In this step, each qubit i is sequentially opened (i.e., set to its gate set point) and, for each flux line in the system, an I_j dependence is performed to determine the I_j values that set $\Phi_i = 0$ and $\Phi_i = \Phi_0$, as indicated in Fig. 7. As a result of this calibration, a flux crosstalk matrix can be defined [109], analogously to how virtual gates are used in semiconducting spin qubits [100,101], and by inverting the crosstalk matrix the unwanted flux crosstalk can be canceled.

VII. DISCUSSION AND CONCLUSIONS

In the preceding sections, we have discussed the potential of highly connected Andreev spin qubits for quantum computing and quantum simulation tasks. Our analysis has focused on an estimation of the coupling strength to first order in $E_{\mathrm{SO},i}/E_J$, as detailed in Sec. III. However, it is crucial to consider the contribution of the spin-dependent inductance of each ASQ, which becomes significant away from the limit $E_{\mathrm{SO},i}/E_J \to 0$ (see Appendix A). These contributions introduce higher-order coupling terms of the form $J_{ijk}\sigma_i^z\sigma_j^z\sigma_k^z$, with $J_{ijk} = \epsilon_k J_{ij}$, where $\epsilon_k \approx E_{\mathrm{SO},k}/E_J$. For instance, the experimentally realistic values of $E_{\mathrm{SO},i}/h = 300$ MHz and $E_J/h = 30$ GHz discussed in Fig. 3 result in an ON-ON coupling strength of $J_{ij}/h = 6$ MHz and unwanted higher-order coupling terms between

two ON qubits, i and j, and an OFF qubit, k, of the order of $J_{ijk}/h = 60$ kHz.

To reduce the $E_{\mathrm{SO},i}/E_J$ ratio and, consequently, mitigate the magnitude of higher-order terms, one can reduce the inductance of the coupling junction. A reduction to $E_{\mathrm{SO},i}/E_J = 1/1000$ within experimentally attainable parameters can be realized by setting $E_{\mathrm{SO},i}/h = 1$ GHz and $E_J/h = 1000$ GHz. This, in turn, sets the ON-ON coupling to $J_{ij}/h = 2$ MHz. Under these conditions, the higher-order coupling terms have an amplitude of $J_{ijk}/h = 2$ kHz. This magnitude of E_J can be achieved by replacing the coupling junction with a linear inductor and using a resonator, instead of a transmon or fluxonium, for readout [43,50,82,84,110]. Note that the reduced coupling strength in this regime leads to slower dynamics and calls for qubit coherence higher than that of previous ASQ implementations [43–45].

These higher-order terms reduce the CPHASE-gate fidelity, imposing a constraint, N_{max}, on the maximum number of qubits in the system. As described in Ref. [111], we can estimate the contribution of these third-order couplings to the infidelity of a CPHASE gate between qubits i and j, to second order, as

$$1 - F_{\mathrm{CZ}} = \sum_{k\neq i,j} (0.25J_{ik}^2 + 0.25J_{jk}^2 + 0.1875J_{ijk}^2 + 0.25J_{ik}J_{ijk} + 0.25J_{jk}J_{ijk}).$$

In particular, if $J_{ijk}/J_{ij} = \epsilon$ for all qubits, we expect a two-qubit gate infidelity of $1 - F_{\mathrm{CZ}} = 0.1875((N-2)\epsilon\pi)^2$. For $\epsilon = 0.001$, this results in $N_{\mathrm{max},99} = 737$ and $N_{\mathrm{max},99.9} = 234$ for target gate fidelities of 99.0% and 99.9%, respectively. Moreover, as discussed in Sec. III, imprecise flux control would lead to residual ON-OFF couplings, further reducing the gate fidelity. If $J_{ijk}/J_{ij} = J_{ik}/J_{ij} = J_{jk}/J_{ij} = \epsilon$, the gate infidelity is $1.1875((N-2)\epsilon\pi)^2$ which, for $\epsilon = 0.001$, limits the number of qubits to $N_{\mathrm{max},99} = 294$ or $N_{\mathrm{max},99.9} = 94$ for the same target gate fidelities.

Another aspect that sets a constraint on the maximum number of qubits in the system is the total required measurement time for the sequential-readout scheme, which increases linearly with the qubit count as $t_{\mathrm{int}}N$. Here, t_{int} denotes the single-shot integration time and we have disregarded the negligible flux pulsing time between the readout of consecutive qubits. This linear scaling of the total readout time poses a limitation once it becomes comparable to the ASQ decay time. Note that the ASQ dephasing time does not play a role during sequential readout, as the qubits waiting to be measured idle in the Z basis. Previous implementations of Andreev spin qubits in InAs have used t_{int} values of the order of 1 µs [43–45,82] and have shown spin decay times of up to 40–50 µs [44,82]. These values would impose a limit on the order of $N_{\mathrm{max}} \approx 10$ for sequential readout. Increasing this constraint would require future generations of ASQs to attain decay times similar to those of state-of-the-art superconducting qubits and semiconductor spin qubits, on the order of 1 ms [112–116]. These decay times would significantly increase the limit on N_{max} set by sequential readout to make it comparable to the constraints imposed by third-order coupling terms and thus mitigating it as a concern.

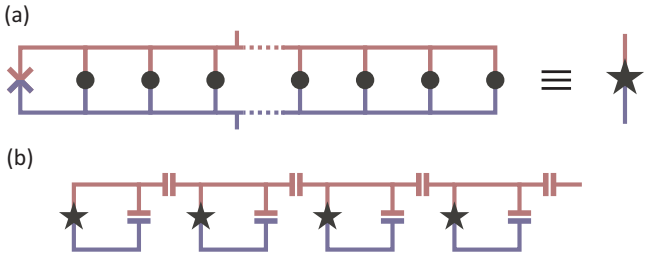

FIG. 8. Quantum computing with superconducting spin qubits. (a) One cluster of N coupled ASQs is represented with a star symbol. (b) Each cluster is read out with a transmon circuit. Different clusters are capacitively coupled to each other to mediate intercluster coupling.

To scale up beyond this limit, we envision defining independent unit cells, each containing N_{max} qubits, as illustrated in Fig. 8(a). A potential architecture for coupling different clusters to each other involves capacitively coupling the readout circuits of two separate clusters [Fig. 8(b)]. This hierarchical approach provides a scalable path for creating larger quantum processors while mitigating the impact of higher-order coupling terms.

To conclude, we have presented an approach for scaling up Andreev spin qubits in a highly connected way. Our work demonstrates the ability to control the magnitude of the coupling strength between any pair of qubits, independently of their physical distance, by varying the applied flux. This feature enables the realization of fast two-qubit gates across the entire system. Moreover, as all couplings can be made of the longitudinal type, the coupling strength remains independent of the relative qubit frequencies. This characteristic offers great flexibility for increasing the qubit count without encountering issues associated with frequency crowding.

When it comes to gate-based digital quantum computation, this enhanced qubit connectivity opens up opportunities for exploring alternative quantum error-correction codes, potentially requiring fewer physical qubits per logical qubit compared to existing surface codes [34]. Regarding analog quantum simulation of Ising systems, the all-to-all connectivity extends the range of NP-hard problems that can be simulated in solid-state qubit platforms without the need for additional qubit overhead to encode the relevant problems, presenting an advantageous alternative to other superconducting-qubit approaches. We note, moreover, that the approach presented here could be generalized

to achieve all-to-all qubit connectivity via inductive coupling for other flux-based superconducting qubits, such as the fluxonium qubit [74], or alternatively for bosonic qubits, providing more straightforward tunability and scaling compared to prior work [37].

ACKNOWLEDGMENTS

We thank P. McMahon, B. van Heck, and V. Fatemi for discussions and their feedback on this paper. This work is cofunded by Microsoft Corporation. C.K.A. acknowledges support from the Dutch Research Council (NWO) and from the Horizon Europe Framework Program of the European Commission through the European Innovation Council Pathfinder Grant No. 101115315 (QuKiT).

APPENDIX A: HIGHER-ORDER LONGITUDINAL COUPLING TERMS

Away from the limit $E_{\mathrm{SO},i}/E_J \to 0$, it becomes essential to account for modifications to the coupling described in Eq. (6) due to the presence of a state-dependent parallel inductance. This inductance introduces a modification to $\tilde{E}$, resulting in

$$\tilde{E} = E_J + \sum_{l=1}^{N} E_{J,l} e^{i\sum_{k=1}^{l}\varphi_k} + \sum_{l=1}^{N} \sigma_l^z E_{\mathrm{SO},l} e^{i\left(\frac{\pi}{2}+\sum_{k=1}^{l}\varphi_k\right)}. \tag{A1}$$

The $E_{\mathrm{SO},i}/E_J$ term gives rise to higher-order coupling terms of the form $\sigma_i^z\sigma_j^z\sigma_k^z$ that can be found by Taylor expanding Eq. (6) around $E_{\mathrm{SO},i}/E_J = 0$. The second-order contribution from the denominator yields

$$J_{ij}^{(2)} = J_{ij}^{(1)}\left(1 - \sum_{l=1}^{N} \frac{E_{\mathrm{SO},l}}{E_J}\sigma_l^z e^{i\left(\frac{\pi}{2}+\sum_{k=1}^{l}\varphi_k\right)}\right), \tag{A2}$$

where $J_{ij}^{(1)}$ is the first-order approximation from Eq. (6). This results in a contribution to the three-qubit coupling terms, $J_{ijk}\sigma_i^z\sigma_j^z\sigma_k^z$, that is a factor of $E_J/E_{\mathrm{SO},k}$ times smaller than the two-qubit coupling terms J_{ij} (i.e., $J_{ijk} = E_{\mathrm{SO},k}/E_J J_{ij}$).

Additionally, Eq. (A1) results in a σ_k^z-dependent contribution to $\varphi_{\tilde{E}}$. This contribution can be as high as

$$\varphi_{\tilde{E}} = \tan^{-1}\left(\sum_{k=1}^{N}\frac{E_{\mathrm{SO},k}}{E_J}\sigma_k^z\right) \approx \sum_{k=1}^{N}\frac{E_{\mathrm{SO},k}}{E_J}\sigma_k^z \tag{A3}$$

when all qubits are OFF. Here, the approximation is again made to first order in $E_{\mathrm{SO},k}/E_J$. Similarly, this introduces a second contribution to the three-qubit coupling terms, again given by

$$J_{ijk} = J_{ij}\frac{E_{\mathrm{SO},k}}{E_J}. \tag{A4}$$

Once again, this term is scaled by a factor of $E_{\mathrm{SO},k}/E_J$ compared to the two-qubit coupling terms.

APPENDIX B: TRANSVERSE COUPLING UNDER THE PRESENCE OF A PERPENDICULAR ZEEMAN FIELD

For the sake of simplicity and without loss of generality, we consider the case $N = 2$. The Hamiltonian of the coupled ASQ system, expressed in the eigenbasis of the system at zero magnetic field and disregarding spin-independent terms, is given by

$$H_{\mathrm{ASQ}} = \frac{1}{2}E_1\sigma_1^z + \frac{1}{2}E_2\sigma_2^z + \frac{1}{2}J_{12}\sigma_1^z\sigma_2^z. \tag{B1}$$

If a perpendicular magnetic field is applied, the qubit eigenstates are no longer the same. In particular, the Hamiltonian of ASQ*i* becomes

$$H_i(\phi_i) = E_{J,i}\sigma_i^0\cos(\phi_i) - E_{\mathrm{SO},i}\sigma_i^z\sin(\phi_i) \tag{B2}$$

$$+ \frac{1}{2}E_{\mathrm{Z},i}\cos(\theta_i)\sigma_i^z + \frac{1}{2}E_{\mathrm{Z},i}\sin(\theta_i)\sigma_i^x, \tag{B3}$$

where $E_{\mathrm{Z},i}$ represents the magnitude of the Zeeman field and θ_i is the angle between the direction of the external Zeeman field and the zero-field spin direction of ASQ*i*. In the limit of $E_{\mathrm{Z},i} \gg E_{\mathrm{SO},i}$, the eigenstates of ASQ*i*, expressed in its zero-field basis, become

$$\left|\overline{\downarrow_i}\right\rangle = \left(\cos\left(\frac{\theta_i}{2}\right), \sin\left(\frac{\theta_i}{2}\right)\right) \text{ and} \tag{B4}$$

$$\left|\overline{\uparrow_i}\right\rangle = \left(-\sin\left(\frac{\theta_i}{2}\right), \cos\left(\frac{\theta_i}{2}\right)\right). \tag{B5}$$

Consequently, the zero-field σ_i^z and σ_i^x, expressed in the new $\left\{\left|\overline{\downarrow_i}\right\rangle, \left|\overline{\uparrow_i}\right\rangle\right\}$ basis, become

$$\sigma_i^z = \cos(\theta_i)\sigma_i^{\bar{z}} + \sin(\theta_i)\sigma_i^{\bar{x}}, \tag{B6}$$

$$\sigma_i^x = \cos(\theta_i)\sigma_i^{\bar{x}} + \sin(\theta_i)\sigma_i^{\bar{z}}, \tag{B7}$$

where $\sigma_i^{\bar{z}} = \left|\overline{\uparrow_i}\right\rangle\left\langle\overline{\uparrow_i}\right| - \left|\overline{\downarrow_i}\right\rangle\left\langle\overline{\downarrow_i}\right|$ and $\sigma_i^{\bar{x}} = \left|\overline{\uparrow_i}\right\rangle\left\langle\overline{\downarrow_i}\right| + \left|\overline{\downarrow_i}\right\rangle\left\langle\overline{\uparrow_i}\right|$. This leads to the coupling Hamiltonian, expressed in

the new spin eigenbasis

$$\begin{aligned} H_{\mathrm{ASQ}} = & \frac{1}{2}E_1\sigma_1^{\bar{z}} + \frac{1}{2}E_2\sigma_2^{\bar{z}} \\ & + \frac{1}{2}J_{12}\cos(\theta_1)\cos(\theta_2)\sigma_1^{\bar{z}}\sigma_2^{\bar{z}} \\ & + \frac{1}{2}J_{12}\sin(\theta_1)\cos(\theta_2)\sigma_1^{\bar{x}}\sigma_2^{\bar{z}} \\ & + \frac{1}{2}J_{12}\cos(\theta_1)\sin(\theta_2)\sigma_1^{\bar{z}}\sigma_2^{\bar{x}} \\ & + \frac{1}{2}J_{12}\sin(\theta_1)\sin(\theta_2)\sigma_1^{\bar{x}}\sigma_2^{\bar{x}}. \end{aligned} \tag{B8}$$

This expression comprises both transversal (XX) and longitudinal (ZZ) coupling terms, along with ZX and XZ terms, with amplitudes

$$J_{12}^{zz} = J_{12}\cos(\theta_1)\cos(\theta_2), \tag{B9}$$

$$J_{12}^{xz} = J_{12}\sin(\theta_1)\cos(\theta_2), \tag{B10}$$

$$J_{12}^{zx} = J_{12}\cos(\theta_1)\sin(\theta_2), \quad \text{and} \tag{B11}$$

$$J_{12}^{xx} = J_{12}\sin(\theta_1)\sin(\theta_2). \tag{B12}$$

If the Zeeman field is perpendicular to both qubits, $\theta_1 = \theta_2 = \pi/2$, the longitudinal, the XZ and ZX terms vanish, leaving only the transverse coupling term with an amplitude of $J_{12}^{xx} = J_{12}$.

[1] S. G. J. Philips, M. T. Madzik, S. V. Amitonov, S. L. de Snoo, M. Russ, N. Kalhor, C. Volk, W. I. L. Lawrie, D. Brousse, L. Tryputen, B. P. Wuetz, A. Sammak, M. Veldhorst, G. Scappucci, and L. M. K. Vandersypen, Universal control of a six-qubit quantum processor in silicon, Nature **609**, 919 (2022).

[2] F. Borsoi, N. W. Hendrickx, V. John, M. Meyer, S. Motz, F. van Riggelen, A. Sammak, S. L. de Snoo, G. Scappucci, and M. Veldhorst, Shared control of a 16 semiconductor quantum dot crossbar array, Nat. Nanotechnol. **19**, 21 (2023).

[3] C.-A. Wang, V. John, H. Tidjani, C. X. Yu, A. S. Ivlev, C. Déprez, F. van Riggelen-Doelman, B. D. Woods, N. W. Hendrickx, W. I. L. Lawrie, L. E. A. Stehouwer, S. D. Oosterhout, A. Sammak, M. Friesen, G. Scappucci, S. L. de Snoo, M. Rimbach-Russ, F. Borsoi, and M. Veldhorst, Operating semiconductor quantum processors with hopping spins, Science **385**, 447 (2024).

[4] S. Neyens, *et al.*, Probing single electrons across 300-mm spin qubit wafers, Nature **629**, 80 (2024).

[5] Y. Kim, A. Eddins, S. Anand, K. X. Wei, E. van den Berg, S. Rosenblatt, H. Nayfeh, Y. Wu, M. Zaletel, K. Temme, and A. Kandala, Evidence for the utility of quantum computing before fault tolerance, Nature **618**, 500 (2023).

[6] O. Shtanko, D. S. Wang, H. Zhang, N. Harle, A. Seif, R. Movassagh, and Z. Minev, Uncovering local integrability in quantum many-body dynamics, arXiv:2307.07552.

[7] F. Arute, *et al.*, Quantum supremacy using a programmable superconducting processor, Nature **574**, 505 (2019).

[8] Google Quantum AI, Phase transition in random circuit sampling, arXiv:2304.11119.

[9] Google Quantum AI, Suppressing quantum errors by scaling a surface code logical qubit, Nature **614**, 676 (2023).

[10] A. R. Mills, C. R. Guinn, M. J. Gullans, A. J. Sigillito, M. M. Feldman, E. Nielsen, and J. R. Petta, Two-qubit silicon quantum processor with operation fidelity exceeding 99%, Sci. Adv. **8**, eabn5130 (2022).

[11] X. Xue, M. Russ, N. Samkharadze, B. Undseth, A. Sammak, G. Scappucci, and L. M. K. Vandersypen, Quantum logic with spin qubits crossing the surface code threshold, Nature **601**, 343 (2022).

[12] A. Noiri, K. Takeda, T. Nakajima, T. Kobayashi, A. Sammak, G. Scappucci, and S. Tarucha, Fast universal quantum gate above the fault-tolerance threshold in silicon, Nature **601**, 338 (2022).

[13] M. T. Madzik, *et al.*, Precision tomography of a three-qubit donor quantum processor in silicon, Nature **601**, 348 (2022).

[14] Y.-H. Wu, L. C. Camenzind, A. Noiri, K. Takeda, T. Nakajima, T. Kobayashi, C.-Y. Chang, A. Sammak, G. Scappucci, H.-S. Goan, and S. Tarucha, Hamiltonian phase error in resonantly driven CNOT gate above the fault-tolerant threshold, npj Quantum Inf. **10**, 8 (2024).

[15] T. Tanttu, *et al.*, Assessment of the errors of high-fidelity two-qubit gates in silicon quantum dots, Nat. Phys. **20**, 1804 (2024).

[16] Y. Sung, L. Ding, J. Braumüller, A. Vepsäläinen, B. Kannan, M. Kjaergaard, A. Greene, G. O. Samach, C. McNally, D. Kim, A. Melville, B. M. Niedzielski, M. E. Schwartz, J. L. Yoder, T. P. Orlando, S. Gustavsson, and W. D. Oliver, Realization of high-fidelity CZ and zz-free iSWAP gates with a tunable coupler, Phys. Rev. X **11**, 021058 (2021).

[17] L. Ding, M. Hays, Y. Sung, B. Kannan, J. An, A. Di Paolo, A. H. Karamlou, T. M. Hazard, K. Azar, D. K. Kim, B. M. Niedzielski, A. Melville, M. E. Schwartz, J. L. Yoder, T. P. Orlando, S. Gustavsson, J. A. Grover, K. Serniak, and W. D. Oliver, High-fidelity, frequency-flexible two-qubit fluxonium gates with a transmon coupler, Phys. Rev. X **13**, 031035 (2023).

[18] S. Sheldon, E. Magesan, J. M. Chow, and J. M. Gambetta, Procedure for systematically tuning up cross-talk in the cross-resonance gate, Phys. Rev. A **93**, 060302 (2016).

[19] S. S. Hong, A. T. Papageorge, P. Sivarajah, G. Crossman, N. Didier, A. M. Polloreno, E. A. Sete, S. W. Turkowski, M. P. da Silva, and B. R. Johnson, Demonstration of a parametrically activated entangling gate protected from flux noise, Phys. Rev. A **101**, 012302 (2020).

[20] F. Marxer, *et al.*, Long-distance transmon coupler with CZ-gate fidelity above 99.8, PRX Quantum **4**, 010314 (2023).

[21] L. M. K. Vandersypen, H. Bluhm, J. S. Clarke, A. S. Dzurak, R. Ishihara, A. Morello, D. J. Reilly, L. R. Schreiber, and M. Veldhorst, Interfacing spin qubits in quantum dots

and donors—hot, dense, and coherent, npj Quantum Inf. **3**, 34 (2017).

[22] R. Li, L. Petit, D. P. Franke, J. P. Dehollain, J. Helsen, M. Steudtner, N. K. Thomas, Z. R. Yoscovits, K. J. Singh, S. Wehner, L. M. K. Vandersypen, J. S. Clarke, and M. Veldhorst, A crossbar network for silicon quantum dot qubits, Sci. Adv. **4**, eaar3960 (2018).

[23] M. Tadokoro, T. Nakajima, T. Kobayashi, K. Takeda, A. Noiri, K. Tomari, J. Yoneda, S. Tarucha, and T. Kodera, Designs for a two-dimensional Si quantum dot array with spin qubit addressability, Sci. Rep. **11**, 19406 (2021).

[24] J. M. Boter, J. P. Dehollain, J. P. van Dijk, Y. Xu, T. Hensgens, R. Versluis, H. W. Naus, J. S. Clarke, M. Veldhorst, F. Sebastiano, and L. M. Vandersypen, Spiderweb array: A sparse spin-qubit array, Phys. Rev. Appl. **18**, 024053 (2022).

[25] L. B. Nguyen, G. Koolstra, Y. Kim, A. Morvan, T. Chistolini, S. Singh, K. N. Nesterov, C. Jünger, L. Chen, Z. Pedramrazi, B. K. Mitchell, J. M. Kreikebaum, S. Puri, D. I. Santiago, and I. Siddiqi, Blueprint for a high-performance fluxonium quantum processor, PRX Quantum **3**, 037001 (2022).

[26] R. Versluis, S. Poletto, N. Khammassi, B. Tarasinski, N. Haider, D. J. Michalak, A. Bruno, K. Bertels, and L. DiCarlo, Scalable quantum circuit and control for a superconducting surface code, Phys. Rev. Appl. **8**, 034021 (2017).

[27] C. Chamberland, G. Zhu, T. J. Yoder, J. B. Hertzberg, and A. W. Cross, Topological and subsystem codes on low-degree graphs with flag qubits, Phys. Rev. X **10**, 011022 (2020).

[28] Y. Makhlin, G. Scöhn, and A. Shnirman, Josephson-junction qubits with controlled couplings, Nature **398**, 305 EP (1999).

[29] Y. Makhlin, G. Shön, and A. Shnirman, Nano-electronic realizations of quantum bits, J. Low Temp. Phys. **118**, 751 (2000).

[30] T. Onodera, E. Ng, and P. L. McMahon, A quantum annealer with fully programmable all-to-all coupling via Floquet engineering, npj Quantum Inf. **6**, 48 (2020).

[31] B. Marinelli, J. Luo, H. Ren, B. M. Niedzielski, D. K. Kim, R. Das, M. Schwartz, D. I. Santiago, and I. Siddiqi, Dynamically reconfigurable photon exchange in a superconducting quantum processor, arXiv:2303.03507.

[32] S. B. Bravyi and A. Y. Kitaev, Quantum codes on a lattice with boundary, arXiv:9811052.

[33] E. Dennis, A. Kitaev, A. Landahl, and J. Preskill, Topological quantum memory, J. Math. Phys. **43**, 4452 (2002).

[34] S. Bravyi, A. W. Cross, J. M. Gambetta, D. Maslov, P. Rall, and T. J. Yoder, High-threshold and low-overhead fault-tolerant quantum memory, Nature **627**, 778 (2024).

[35] W. Lechner, P. Hauke, and P. Zoller, A quantum annealing architecture with all-to-all connectivity from local interactions, Sci. Adv. **1**, e1500838 (2015).

[36] M. Leib, P. Zoller, and W. Lechner, A transmon quantum annealer: Decomposing many-body Ising constraints into pair interactions, Quantum Sci. Technol. **1**, 015008 (2016).

[37] S. E. Nigg, N. Lörch, and R. P. Tiwari, Robust quantum optimizer with full connectivity, Sci. Adv. **3**, e1602273 (2017).

[38] S. Puri, C. K. Andersen, A. L. Grimsmo, and A. Blais, Quantum annealing with all-to-all connected nonlinear oscillators, Nat. Commun. **8**, 15785 (2017).

[39] E. Bäumer, V. Tripathi, D. S. Wang, P. Rall, E. H. Chen, S. Majumder, A. Seif, and Z. K. Minev, Efficient long-range entanglement using dynamic circuits, PRX Quantum **5**, 030339 (2024).

[40] N. M. Chtchelkatchev and Y. V. Nazarov, Andreev quantum dots for spin manipulation, Phys. Rev. Lett. **90**, 226806 (2003).

[41] C. Padurariu and Y. V. Nazarov, Theoretical proposal for superconducting spin qubits, Phys. Rev. B **81**, 144519 (2010).

[42] S. Park and A. L. Yeyati, Andreev spin qubits in multichannel Rashba nanowires, Phys. Rev. B **96**, 125416 (2017).

[43] M. Hays, V. Fatemi, D. Bouman, J. Cerrillo, S. Diamond, K. Serniak, T. Connolly, P. Krogstrup, J. Nygård, A. L. Yeyati, A. Geresdi, and M. H. Devoret, Coherent manipulation of an Andreev spin qubit, Science **373**, 430 (2021).

[44] M. Pita-Vidal, A. Bargerbos, R. Žitko, L. J. Splitthoff, L. Grünhaupt, J. J. Wesdorp, Y. Liu, L. P. Kouwenhoven, R. Aguado, B. van Heck, A. Kou, and C. K. Andersen, Direct manipulation of a superconducting spin qubit strongly coupled to a transmon qubit, Nat. Phys. **19**, 1110 (2023).

[45] M. Pita-Vidal, J. J. Wesdorp, L. J. Splitthoff, A. Bargerbos, Y. Liu, L. P. Kouwenhoven, and C. K. Andersen, Strong tunable coupling between two distant superconducting spin qubits, Nat. Phys. **20**, 1158 (2024).

[46] M. Spethmann, X.-P. Zhang, J. Klinovaja, and D. Loss, Coupled superconducting spin qubits with spin-orbit interaction, Phys. Rev. B **106**, 115411 (2022).

[47] S. Hoffman, M. Hays, K. Serniak, T. Hazard, and C. Tahan, Decoherence in Andreev spin qubits, arXiv:2403.00710.

[48] L. Y. Cheung, R. Haller, A. Kononov, C. Ciaccia, J. H. Ungerer, T. Kanne, J. Nygård, P. Winkel, T. Reisinger, I. M. Pop, A. Baumgartner, and C. Schönenberger, Photon-mediated long range coupling of two Andreev level qubits, arXiv:2310.15995.

[49] E. J. H. Lee, X. Jiang, R. Žitko, R. Aguado, C. M. Lieber, and S. De Franceschi, Scaling of subgap excitations in a superconductor-semiconductor nanowire quantum dot, Phys. Rev. B **95**, 180502 (2017).

[50] V. Fatemi, P. D. Kurilovich, M. Hays, D. Bouman, T. Connolly, S. Diamond, N. E. Frattini, V. D. Kurilovich, P. Krogstrup, J. Nygård, A. Geresdi, L. I. Glazman, and M. H. Devoret, Microwave susceptibility observation of interacting many-body Andreev states, Phys. Rev. Lett. **129**, 227701 (2022).

[51] P. D. Kurilovich, V. D. Kurilovich, V. Fatemi, M. H. Devoret, and L. I. Glazman, Microwave response of an Andreev bound state, Phys. Rev. B **104**, 174517 (2021).

[52] A. Bargerbos, M. Pita-Vidal, R. Žitko, J. Ávila, L. J. Splitthoff, L. Grünhaupt, J. J. Wesdorp, C. K. Andersen, Y. Liu, L. P. Kouwenhoven, R. Aguado, A. Kou, and B. van Heck, Singlet-doublet transitions of a quantum dot Josephson junction detected in a transmon circuit, PRX Quantum **3**, 030311 (2022).

[53] F. J. Matute-Cañadas, C. Metzger, S. Park, L. Tosi, P. Krogstrup, J. Nygård, M. F. Goffman, C. Urbina, H. Pothier, and A. L. Yeyati, Signatures of interactions in the Andreev spectrum of nanowire Josephson junctions, Phys. Rev. Lett. **128**, 197702 (2022).

[54] L. Pavešić, R. Aguado, and R. Žitko, Strong-coupling theory of quantum-dot Josephson junctions: Role of a residual quasiparticle, Phys. Rev. B **109**, 125131 (2024).

[55] M. R. Sahu, F. J. Matute-Cañadas, M. Benito, P. Krogstrup, J. Nygård, M. F. Goffman, C. Urbina, A. L. Yeyati, and H. Pothier, Ground-state phase diagram and parity-flipping microwave transitions in a gate-tunable Josephson junction, Phys. Rev. B **109**, 134506 (2024).

[56] L. Lakic, W. I. L. Lawrie, D. van Driel, L. E. A. Stehouwer, M. Veldhorst, G. Scappucci, F. Kuemmeth, and A. Chatterjee, A proximitized quantum dot in germanium, arXiv:2405.02013.

[57] A. Bargerbos, M. Pita-Vidal, R. Žitko, L. J. Splitthoff, L. Grünhaupt, J. J. Wesdorp, Y. Liu, L. P. Kouwenhoven, R. Aguado, C. K. Andersen, A. Kou, and B. van Heck, Spectroscopy of spin-split Andreev levels in a quantum dot with superconducting leads, Phys. Rev. Lett. **131**, 097001 (2023).

[58] W. Ha, S. D. Ha, M. D. Choi, Y. Tang, A. E. Schmitz, M. P. Levendorf, K. Lee, J. M. Chappell, T. S. Adams, D. R. Hulbert, E. Acuna, R. S. Noah, J. W. Matten, M. P. Jura, J. A. Wright, M. T. Rakher, and M. G. Borselli, A flexible design platform for Si/SiGe exchange-only qubits with low disorder, Nano Lett. **22**, 1443 (2022).

[59] D. R. W. Yost, M. E. Schwartz, J. Mallek, D. Rosenberg, C. Stull, J. L. Yoder, G. Calusine, M. Cook, R. Das, A. L. Day, E. B. Golden, D. K. Kim, A. Melville, B. M. Niedzielski, W. Woods, A. J. Kerman, and W. D. Oliver, Solid-state qubits integrated with superconducting through-silicon vias, npj Quantum Inf. **6**, 59 (2020).

[60] Y. J. Y. Lankwarden, A. Endo, J. J. A. Baselmans, and M. P. Bruijn, Development of NbTiN-Al direct antenna coupled kinetic inductance detectors, J. Low Temp. Phys. **167**, 367 (2012).

[61] Z. Chen, A. Megrant, J. Kelly, R. Barends, J. Bochmann, Y. Chen, B. Chiaro, A. Dunsworth, E. Jeffrey, J. Y. Mutus, P. J. J. O'Malley, C. Neill, P. Roushan, D. Sank, A. Vainsencher, J. Wenner, T. C. White, A. N. Cleland, and J. M. Martinis, Fabrication and characterization of aluminum airbridges for superconducting microwave circuits, Appl. Phys. Lett. **104**, 052602 (2014).

[62] D. Rosenberg, D. Kim, R. Das, D. Yost, S. Gustavsson, D. Hover, P. Krantz, A. Melville, L. Racz, G. O. Samach, S. J. Weber, F. Yan, J. L. Yoder, A. J. Kerman, and W. D. Oliver, 3D integrated superconducting qubits, npj Quantum Inf. **3**, 42 (2017).

[63] M. Hinderling, S. C. ten Kate, M. Coraiola, D. Haxell, M. Stiefel, M. Mergenthaler, S. Paredes, S. Bedell, D. Sabonis, and F. Nichele, Direct microwave spectroscopy of Andreev bound states in planar Ge Josephson junctions, PRX Quantum **5**, 030357 (2024).

[64] M. Valentini, O. Sagi, L. Baghumyan, T. de Gijsel, J. Jung, S. Calcaterra, A. Ballabio, J. Aguilera Servin, K. Aggarwal, M. Janik, T. Adletzberger, R. Seoane Souto, M. Leijnse, J. Danon, C. Schrade, E. Bakkers, D. Chrastina, G. Isella, and G. Katsaros, Parity-conserving Cooper-pair transport and ideal superconducting diode in planar germanium, Nat. Commun. **15**, 169 (2024).

[65] O. Sagi, A. Crippa, M. Valentini, M. Janik, L. Baghumyan, G. Fabris, L. Kapoor, F. Hassani, J. Fink, S. Calcaterra, D. Chrastina, G. Isella, and G. Katsaros, A gate tunable transmon qubit in planar Ge, Nat. Commun. **15**, 6400 (2024).

[66] J. Cerrillo, M. Hays, V. Fatemi, and A. L. Yeyati, Spin coherent manipulation in Josephson weak links, Phys. Rev. Res. **3**, L022012 (2021).

[67] L. Pavešić and R. Žitko, Generalized transmon Hamiltonian for Andreev spin qubits, Phys. Rev. B **109**, 155164 (2024).

[68] Y. Fauvel, J. S. Meyer, and M. Houzet, Opportunities for the direct manipulation of a phase-driven Andreev spin qubit, Phys. Rev. B **109**, 184515 (2024).

[69] V. N. Golovach, M. Borhani, and D. Loss, Electric-dipole-induced spin resonance in quantum dots, Phys. Rev. B **74**, 165319 (2006).

[70] K. C. Nowack, F. H. L. Koppens, Y. V. Nazarov, and L. M. K. Vandersypen, Coherent control of a single electron spin with electric fields, Science **318**, 1430 (2007).

[71] Note that sizable (compared to $E_{\mathrm{SO},i}$) perpendicular Zeeman components might introduce undesired transverse coupling terms between ASQs. See Appendix B.

[72] J. Wesdorp, *et al.*, Microwave spectroscopy of Andreev bound states in InSb-Al nanowire Josephson junctions defined using shadow-wall lithography in a circuit-QED architecture, In preparation (2024).

[73] Yokogawa, GS610 Source Measure Unit User's manual (2021), [Online; accessed 27-September-2023] https://cdn.tmi.yokogawa.com/1/6104/files/IM765501-01E.pdf.

[74] X. Ma, *et al.*, Native approach to controlled-z gates in inductively coupled fluxonium qubits, Phys. Rev. Lett. **132**, 060602 (2024).

[75] D. C. McKay, C. J. Wood, S. Sheldon, J. M. Chow, and J. M. Gambetta, Efficient Z gates for quantum computing, Phys. Rev. A **96**, 022330 (2017).

[76] M. Rol, F. Battistel, F. Malinowski, C. Bultink, B. Tarasinski, R. Vollmer, N. Haider, N. Muthusubramanian, A. Bruno, B. Terhal, and L. DiCarlo, Fast, high-fidelity conditional-phase gate exploiting leakage interference in weakly anharmonic superconducting qubits, Phys. Rev. Lett. **123**, 120502 (2019).

[77] H. Zhang, S. Chakram, T. Roy, N. Earnest, Y. Lu, Z. Huang, D. K. Weiss, J. Koch, and D. I. Schuster, Universal fast-flux control of a coherent, low-frequency qubit, Phys. Rev. X **11**, 011010 (2021).

[78] F. Barahona, On the computational complexity of Ising spin glass models, J. Phys. A Math. Gen. **15**, 3241 (1982).

[79] T. Kadowaki and H. Nishimori, Quantum annealing in the transverse Ising model, Phys. Rev. E **58**, 5355 (1998).

[80] R. D. Somma, D. Nagaj, and M. Kieferová, Quantum speedup by quantum annealing, Phys. Rev. Lett. **109**, 050501 (2012).

[81] T. Albash and D. A. Lidar, Demonstration of a scaling advantage for a quantum annealer over simulated annealing, Phys. Rev. X **8**, 031016 (2018).

[82] M. Hays, V. Fatemi, K. Serniak, D. Bouman, S. Diamond, G. de Lange, P. Krogstrup, J. Nygård, A. Geresdi,

and M. H. Devoret, Continuous monitoring of a trapped superconducting spin, Nat. Phys. **16**, 1103 (2020).

[83] C. Metzger, S. Park, L. Tosi, C. Janvier, A. A. Reynoso, M. F. Goffman, C. Urbina, A. L. Yeyati, and H. Pothier, Circuit-QED with phase-biased Josephson weak links, Phys. Rev. Res. **3**, 013036 (2021).

[84] J. J. Wesdorp, F. J. Matute-Cañadas, A. Vaartjes, L. Grünhaupt, T. Laeven, S. Roelofs, L. J. Splitthoff, M. Pita-Vidal, A. Bargerbos, D. J. van Woerkom, P. Krogstrup, L. P. Kouwenhoven, C. K. Andersen, A. L. Yeyati, B. van Heck, and G. de Lange, Microwave spectroscopy of interacting Andreev spins, Phys. Rev. B **109**, 045302 (2024).

[85] Note that if the $E_{\mathrm{SO},i}/E_J$ ratio needs to be reduced further by increasing E_J to the terahertz range, an alternative readout method involves replacing the coupling junction with a linear inductor and using a readout resonator with a geometry analogous to that in Refs. [43,50,53,55,82–84,110,117].

[86] R. Shillito, A. Petrescu, J. Cohen, J. Beall, M. Hauru, M. Ganahl, A. G. Lewis, G. Vidal, and A. Blais, Dynamics of transmon ionization, Phys. Rev. Appl. **18**, 034031 (2022).

[87] M. F. Dumas, B. Groleau-Paré, A. McDonald, M. H. Muñoz-Arias, C. Lledó, B. D'Anjou, and A. Blais, Unified picture of measurement-induced ionization in the transmon, arXiv:2402.06615.

[88] J. Koch, T. M. Yu, J. Gambetta, A. A. Houck, D. I. Schuster, J. Majer, A. Blais, M. H. Devoret, S. M. Girvin, and R. J. Schoelkopf, Charge-insensitive qubit design derived from the Cooper pair box, Phys. Rev. A **76**, 042319 (2007).

[89] U. Güngördü, R. Ruskov, S. Hoffman, K. Serniak, A. J. Kerman, and C. Tahan, Quantum dynamics of superconductor-quantum dot-superconductor Josephson junctions, arXiv:2402.10330.

[90] A. Bargerbos, L. J. Splitthoff, M. Pita-Vidal, J. J. Wesdorp, Y. Liu, P. Krogstrup, L. P. Kouwenhoven, C. K. Andersen, and L. Grünhaupt, Mitigation of quasiparticle loss in superconducting qubits by phonon scattering, Phys. Rev. Appl. **19**, 024014 (2023).

[91] V. E. Manucharyan, J. Koch, L. I. Glazman, and M. H. Devoret, Fluxonium: Single Cooper-pair circuit free of charge offsets, Science **326**, 113 (2009).

[92] G. Zhu, D. G. Ferguson, V. E. Manucharyan, and J. Koch, Circuit QED with fluxonium qubits: Theory of the dispersive regime, Phys. Rev. B **87**, 024510 (2013).

[93] T. V. Stefanski and C. K. Andersen, Flux-pulse-assisted readout of a fluxonium qubit, Phys. Rev. Appl. **22**, 014079 (2024).

[94] K. N. Nesterov and I. V. Pechenezhskiy, Measurement-induced state transitions in dispersive qubit readout schemes, arXiv:2402.07360.

[95] J. E. Johnson, C. Macklin, D. H. Slichter, R. Vijay, E. B. Weingarten, J. Clarke, and I. Siddiqi, Heralded state preparation in a superconducting qubit, Phys. Rev. Lett. **109**, 050506 (2012).

[96] D. Ristè, J. G. van Leeuwen, H.-S. Ku, K. W. Lehnert, and L. DiCarlo, Initialization by measurement of a superconducting quantum bit circuit, Phys. Rev. Lett. **109**, 050507 (2012).

[97] D. Ristè, M. Dukalski, C. A. Watson, G. de Lange, M. J. Tiggelman, Y. M. Blanter, K. W. Lehnert, R. N. Schouten, and L. DiCarlo, Deterministic entanglement of superconducting qubits by parity measurement and feedback, Nature **502**, 350 (2013).

[98] E. Magesan, J. M. Gambetta, and J. Emerson, Scalable and robust randomized benchmarking of quantum processes, Phys. Rev. Lett. **106**, 180504 (2011).

[99] R. Sagastizabal, X. Bonet-Monroig, M. Singh, M. A. Rol, C. C. Bultink, X. Fu, C. H. Price, V. P. Ostroukh, N. Muthusubramanian, A. Bruno, M. Beekman, N. Haider, T. E. O'Brien, and L. DiCarlo, Experimental error mitigation via symmetry verification in a variational quantum eigensolver, Phys. Rev. A **100**, 010302 (2019).

[100] C. Volk, A. M. J. Zwerver, U. Mukhopadhyay, P. T. Eendebak, C. J. van Diepen, J. P. Dehollain, T. Hensgens, T. Fujita, C. Reichl, W. Wegscheider, and L. M. K. Vandersypen, Loading a quantum-dot based "qubyte" register, npj Quantum Inf. **5**, 29 (2019).

[101] F. K. Unseld, M. Meyer, M. T. Madzik, F. Borsoi, S. L. de Snoo, S. V. Amitonov, A. Sammak, G. Scappucci, M. Veldhorst, and L. M. K. Vandersypen, A 2D quantum dot array in planar ^{28}Si/SiGe, arXiv:2305.19681.

[102] S. E. d. Graaf, A. V. Danilov, A. Adamyan, T. Bauch, and S. E. Kubatkin, Magnetic field resilient superconducting fractal resonators for coupling to free spins, J. Appl. Phys. **112**, 123905 (2012).

[103] N. Samkharadze, A. Bruno, P. Scarlino, G. Zheng, D. P. DiVincenzo, L. DiCarlo, and L. M. K. Vandersypen, High-kinetic-inductance superconducting nanowire resonators for circuit QED in a magnetic field, Phys. Rev. Appl. **5**, 044004 (2016).

[104] J. G. Kroll, F. Borsoi, K. L. van der Enden, W. Uilhoorn, D. de Jong, M. Quintero-Pérez, D. J. van Woerkom, A. Bruno, S. R. Plissard, D. Car, E. P. A. M. Bakkers, M. C. Cassidy, and L. P. Kouwenhoven, Magnetic-field-resilient superconducting coplanar-waveguide resonators for hybrid circuit quantum electrodynamics experiments, Phys. Rev. Appl. **11**, 064053 (2019).

[105] C. W. Zollitsch, J. O'Sullivan, O. Kennedy, G. Dold, and J. J. L. Morton, Tuning high-Q superconducting resonators by magnetic field reorientation, AIP Adv. **9**, 125225 (2019).

[106] D. Feldstein i Bofill, Master's thesis, QuTech, TU Delft, 2022. http://resolver.tudelft.nl/uuid:777aaeac-d4a8-4a5a-ad78-e4d99f6d06c8.

[107] W. Lawrie, Ph.D. thesis, QuTech, TU Delft, 2022.

[108] S. Vaitiekėnas, M.-T. Deng, J. Nygård, P. Krogstrup, and C. M. Marcus, Effective g factor of subgap states in hybrid nanowires, Phys. Rev. Lett. **121**, 037703 (2018).

[109] D. M. Abrams, N. Didier, S. A. Caldwell, B. R. Johnson, and C. A. Ryan, Methods for measuring magnetic flux crosstalk between tunable transmons, Phys. Rev. Appl. **12**, 064022 (2019).

[110] J. J. Wesdorp, L. Grünhaupt, A. Vaartjes, M. Pita-Vidal, A. Bargerbos, L. J. Splitthoff, P. Krogstrup, B. van Heck, and G. de Lange, Dynamical polarization of the fermion parity in a nanowire Josephson junction, Phys. Rev. Lett. **131**, 117001 (2023).

[111] S. Krinner, S. Lazar, A. Remm, C. Andersen, N. Lacroix, G. Norris, C. Hellings, M. Gabureac, C. Eichler, and

A. Wallraff, Benchmarking coherent errors in controlled-phase gates due to spectator qubits, Phys. Rev. Appl. **14**, 024042 (2020).

[112] L. Petit, J. M. Boter, H. G. J. Eenink, G. Droulers, M. L. V. Tagliaferri, R. Li, D. P. Franke, K. J. Singh, J. S. Clarke, R. N. Schouten, V. V. Dobrovitski, L. M. K. Vandersypen, andM. Veldhorst, Spin lifetime and charge noise in hot silicon quantum dot qubits, Phys. Rev. Lett. **121**, 076801 (2018).

[113] W. I. L. Lawrie, N. W. Hendrickx, F. van Riggelen, M. Russ, L. Petit, A. Sammak, G. Scappucci, and M. Veldhorst, Spin relaxation benchmarks and individual qubit addressability for holes in quantum dots, Nano Lett. **20**, 7237 (2020).

[114] C. Wang, *et al.*, Towards practical quantum computers: transmon qubit with a lifetime approaching 0.5 milliseconds, npj Quantum Inf. **8**, 3 (2022).

[115] A. Somoroff, Q. Ficheux, R. A. Mencia, H. Xiong, R. Kuzmin, and V. E. Manucharyan, Millisecond coherence in a superconducting qubit, Phys. Rev. Lett. **130**, 267001 (2023).

[116] M. Bal, *et al.*, Systematic improvements in transmon qubit coherence enabled by niobium surface encapsulation, npj Quantum Inf. **10**, 43 (2024).

[117] L. Tosi, C. Metzger, M. F. Goffman, C. Urbina, H. Pothier, S. Park, A. L. Yeyati, J. Nygård, and P. Krogstrup, Spin-orbit splitting of Andreev states revealed by microwave spectroscopy, Phys. Rev. X **9**, 011010 (2018).